Crystal valley Hall effect

Chao-Yang Tan[1,2], Ze-Feng Gao[1,2], Huan-Cheng Yang[1,2], Zheng-Xin
Liu[1,2], Kai Liu[1,2], Peng-Jie Guo[1,2,*] and Zhong-Yi Lu[1,2,3†]

*1. Department of Physics and Beijing Key Laboratory of Opto-electronic Functional
Materials & Micro-nano Devices. Renmin University of China, Beijing 100872, China*
*2. Key Laboratory of Quantum State Construction and Manipulation (Ministry of Education),
Renmin University of China, Beijing 100872, China and*
3. Hefei National Laboratory, Hefei 230088, China
(Dated: October 2, 2024)

The time-reversal symmetry is thought to be a necessary condition for realizing valley Hall effect.
If the time-reversal symmetry is broken, whether the valley Hall effect can be realized has not been
explored. In this letter, based on symmetry analysis and the first-principles electronic structure
calculations, we demonstrate that the vally Hall effect without time-reversal symmetry can be
realized in two-dimensional altermagnetic materials Fe_2WSe_4 and Fe_2WS_4. Due to crystal symmetry
required, the vally Hall effect without time-reversal symmetry is called crystal vally Hall effect. In
addition, under uniaxial strain, both monolayer Fe_2WSe_4 and Fe_2WS_4 can realize piezomagnetic
effect. Under biaxial compressive stress, both monolayer Fe_2WSe_4 and Fe_2WS_4 will transform
from altermagnetic semiconductor phase to bipolarized topological Weyl semimetal phase. Our
work not only provides a new direction for exploring the novel valley Hall effect, but also provides
a good platform for exploring altermagnetic semiconductors and altermagnetic topological phase
transitions.

Introduction. The time-reversal (T) symmetry results in band degeneracy but opposite Berry curvatures at k and $-k$ in momentum space. For two-dimensional materials, Berry curvature can generate an anomalous velocity perpendicular to the direction of the electric field under an in-plane electric field. If a two-dimensional nonmagnetic insulator without space-inversion symmetry has only two valleys connected by the T symmetry at the Fermi level, the electrons from the two valleys with opposite Berry curvature will move in opposite directions under the in-plane electric field. This is known as valley hall effect. The valley Hall effect has been not only theoretically proposed but also experimentally realized [1–3]. An interesting question is whether the valley Hall effect can still be realized if the T symmetry is broken.

Recently, altermagnetism as a new magnetic phase has been proposed, which is distingushed from ferromagnetism and antiferromagnetism [4–11]. Altermagnetism has the duality of the real-space antiferromagnetism and the reciprocal-space anisotropic spin polarization similar to ferromagnetism. Moreover, altermagnetic materials will break T symmetry under spin-orbital coupling (SOC). Thus, the altermagnetic materials can realize many novel physical effects, such as spin-splitting torque [12–15], giant magnetoresistance (GMR) effect [16, 17], tunneling magnetoresistance (TMR) effect [16, 18], non-trivial superconductivity [19], time-reversal odd anomalous effect [5, 20–25], quantum anomalous Hall effect [11], higher-order topological states [26], Majorana corner modes [27], piezomagnetism effect [28], altermagnetic ferroelectricity [29], strong spin-orbit coupling effect in light element altermagnetic materials [30], quantum crystal valley Hall effect [31] and so on. Remarkably, altermagnetic materials can have valley electrons with opposite spin polarization deriving from crystal symmetry. This provides a possibility for realizing valley Hall effect without the T symmetry.

In this letter, based on symmetry analysis and the first-principles electronic structure calculations, we demonstrate that crystal valley Hall effect can be realized in two-dimensional altermagnetic Fe_2WSe_4 and Fe_2WS_4. Moreover, our calculations show that both monolayer Fe_2WSe_4 and Fe_2WS_4 have magnetic transition temperatures higher than room temperature, which are 340K and 520K, respectively. In addition, under an uniaxial strain, both monolayer Fe_2WSe_4 and Fe_2WS_4 generate valley polarization. Meanwhile, under biaxial compressive stress, a topological phase transition from altermagnetic semiconductor phase to bipolarized Weyl semimetal phase takes place in both monolayer Fe_2WSe_4 and Fe_2WS_4.

Methods. The electronic structure calculations were performed based on the Vienna ab initio simulation package (VASP) [32] with the projector augmented wave (PAW) method [33]. The GGA-PBE exchange-correlation function [34] was used in our calculations. The energy cut-off 600 eV, energy convergence criterion 10^{-6}eV, force convergence criteria 10^{-3}eV/Å, and k-mesh $12 \times 12 \times 1$ (Γ centered Monkhorst-Pack) were used. The dynamical stabilities of Fe_2WX_4 were confirmed by using Phonopy package with the finite displacement method, adopting $3 \times 3 \times 1$ supercell and a $5 \times 5 \times 1$ k-meshes (Γ centered Monkhorst-Pack). The maximally localized Wannier functions were constructed using the wannier90 package [35]. The berry curvature was calculated using postw90 code. Finally, the Monte Carlo

TABLE I. The relative energy (eV) of three different magnetic structures for Fe_2WX_4 (X=S,Se).

Materials	FM	AFM1	AFM2
Fe_2WSe_4	0.514	0	0.146
Fe_2WS_4	0.798	0	0.288

simulations based on the classical Heisenberg model were performed by using the MCSOLVER [36].

Results and analysis. Monolayer Fe_2WX_4 (X=Se,S) takes a square lattice structure with the symmorphic space group P-42m (No.111) symmetry and the corresponding point group is D_{2d} with generators S_{4z} and C_{2x}. Monolayer Fe_2WX_4 contains three atomic layers where Fe and W atomic layer is sandwiched by two X atomic layers as shown in Fig. 1(a) and (b), and the corresponding BZ with high-symmetry points is shown in Fig. 1(c). The crystal parameters of monolayer Fe_2WX_4 are obtained by structural relaxation. The crystal parameters of monolayer Fe_2WSe_4 and Fe_2WS_4 are 5.572 and 5.436 Å, respectively. Then we calculate the phonon spectrum of monolayer Fe_2WX_4, which are shown in Fig. 1(d) and (e). From Fig. 1(d) and (e), the phonon spectrum of both monolayer Fe_2WSe_4 and Fe_2WS_4 have no imaginary frequency. Therefore both monolayer Fe_2WSe_4 and Fe_2WS_4 are dynamically stable. Furhermore, the crystal structure of monolayer Fe_2WX_4 is proposed based on the synthesized layered Cu_2WX_4 (X=S,Se) [37–40], Cu_2MoS_4[41] and Ag_2WS_4 [42], thus it is hopful that monolayer Fe_2WX_4 may be synthesized experimentally.

To determine the magnetic ground states of Fe_2WX_4, we consider three different magnetic configurations including one ferromagnetic (FM) and two antiferromagnetic (AFM1 and AFM2) as shown in Fig. 1(f) and (g) within a $1 \times 2 \times 1$ surpercell. The calculated results show that the AFM1 is magnetic ground state for both monolayer Fe_2WSe_4 and Fe_2WS_4 (Tab. I). Comparing Fig. 1(a) and Fig. 1(f), the magnetic and crystal primitive cells are identical, thus Fe_2WX_4 has no $\left\{ C_2^\perp || \tau \right\}$ spin symmetry. And due to the lack of space-inversion symmetry, Fe_2WX_4 must not have $\left\{ C_2^\perp || I \right\}$ spin symmetry. Meanwhile, the Fe_2WX_4 has $\left\{ C_2^\perp || S_{4z} \right\}$ spin symmetry. Therefore, both Fe_2WSe_4 and Fe_2WS_4 are the d-wave altermagnetic materials.

Then we estimate the Néel temperature for monolayer Fe_2WX_4 by using classical Monte Carlo simulations based on the two-dimensional square lattice Heisenberg model with single-ion anisotropy,

$$H = \sum_{<i,j>} J_1 S_i \cdot S_j + \sum_{<<i,j>>} J_2 S_i \cdot S_j$$
$$+ \sum_{<<i,j>>} J_2' S_i \cdot S_j + A \sum_i |S_i^z|^2 \quad (1)$$

where S_i represents the spin on the i-site, J_1 is the nearest exchange interaction parameter, J_2 and J_2' are the next-nearest exchange interaction parameters with Fe-Fe

channel and with Fe-W-Fe channel, respectively (Fig. 1 (f)). The A is the single-ion magnetic anisotropy with easy-magnetization axes. These exchange interaction parameters were derived from the four-state method which is a mapping analysis of the four magnetic configurations. Based on the Heisenberg model, we calculate Néel temperatures of Fe_2WSe_4 and Fe_2WS_4 by the classical Monte Carlo simulations [36]. The calculated Néel temperatures of Fe_2WSe_4 and Fe_2WS_4 are 340K and 520K, respectively. Thus, the altermagnetic order of monolayer Fe_2WSe_4 and Fe_2WS_4 remains stable at room temperature.

After clarifying the magnetic properties, we investigate the electronic properties of monolayer Fe_2WX_4. From Fig. 1(a), a spin-up (spin-down) Fe atom has W atoms in the y (x) direction but no W atoms in the x (y) direction, so the crystal environment of Fe atoms has strong anisotropy, implying that the polarized charge density of Fe atoms may have strong anisotropy. Our calculations show that the polarization charge density of Fe atoms has indeed strong anisotropy (Fig. 2(a) and (b)), which results in the strong anisotropy of Fe-Fe next neighbor hopping interactions. Moreover, the strong anisotropy of the next nearest neighbor hopping interactions can lead to strong spin splitting in altermagnetic materials [31]. Therefore, altermagnetic monolayer Fe_2WX_4 may have large spin splitting.

Due to $\left\{ C_2^\perp || M_{xy} \right\}$ spin symmetry, all bands of Fe_2WX_4 in the Γ-M direction are spin degenerate. Considering the characteristics of d-wave altermagnetism, all bands at the high-symmetry X and Y points must be spin-splitting and have opposite spins due to $\left\{ C_2^\perp || M_{xy} \right\}$ spin symmetry. To prove our above analysis, we calculated the band structures of monolayer Fe_2WX_4 without SOC, which are shown in Fig. 2(c) and (d). From Fig. 2(c) and (d), both monolayer Fe_2WSe_4 and Fe_2WS_4 are altermagnetic semiconductors with a bandgap being 126 meV and 170 meV, respectively. Moreover, both monolayer Fe_2WSe_4 and Fe_2WS_4 have large spin splits at certain k points in the BZ, such as high-symmetry X and Y points, to be 258 meV and 317 meV, respectively. More importantly, both the bottom of the conduction band and the top of the valence band are at the X and Y points and the corresponding bands have opposite spin polarization. This provides a solid foundation for the realization of crystal valley Hall effect. Due to the $\left\{ C_2^\perp T || C_{2z} T \right\}$ spin symmetry, the Berry curvature is always zero everywhere in the BZ. Then, to realize the crystal valley Hall effect, the SOC effect must be considered for monolayer Fe_2WX_4.

With SOC, the symmetry of monolayer Fe_2WX_4 changes from spin group to magnetic group. Moreover, the magnetic group symmetry depends on the direction of the easy magnetization axis. In order to determine the magnetic group symmetry, we calculated the orientation of the easy magnetization axis of monolayer Fe_2WX_4. The direction of the easy magnetization axis of both monolayer Fe_2WSe_4 and Fe_2WS_4 are along the 001 di-
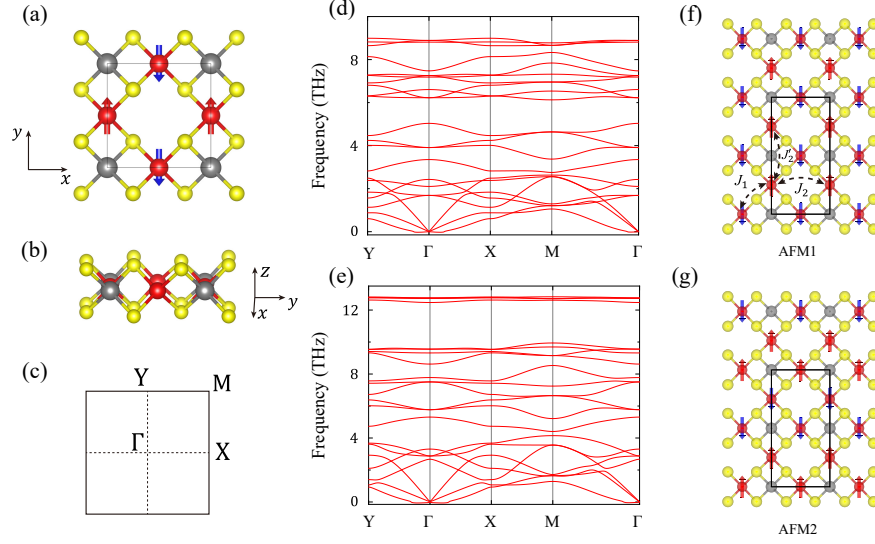
FIG. 1. (a) and (b) represent the top and side views of crystal and magnetic structure of Fe_2WX_4, respectively. The red and blue arrows represent spin-up and spin-down magnetic moments, respectively. (c) The Brillouin zone (BZ) of Fe_2WX_4 where the high-symmetry points are labeled. The phonon dispersion for (d) Fe_2WSe_4 and (e) Fe_2WS_4. (f) and (g) are two antiferromagnetic structures AFM1 and AFM2 for the monolayer Fe_2WX_4, respectively. The index J_1, J_2 and J_2' in (f) denote the diagram of nearest, next-nearest exchange interaction parameters.
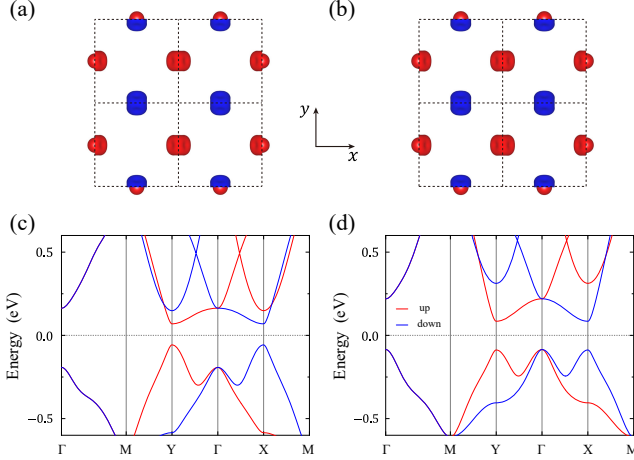

FIG. 2. (a) and (b) are the polarization charge density around the Fe atoms for Fe_2WSe_4 and Fe_2WS_4 without SOC (red: spin-up, blue: spin-down), respectively. (c) and (d) are electronic band structure of Fe_2WSe_4 and Fe_2WS_4 along the high-symmetry lines without SOC, respectively.

rection. So, both monolayer Fe_2WSe_4 and Fe_2WS_4 have $2S_{4z}T$, C_{2z}, $C_{2x}T$, $C_{2y}T$ and $2M_{xy}$ symmetry. The mirror M_{xy} or $S_{4z}T$ symmetry can protect energy degeneracy and opposite Berry curvature at the high-symmetry X and Y points (Fig. 3(a) and (b)). Moreover, the high-symmetry X and Y points still have opposite spin polarization under SOC ((Fig. 3(a) and (b))). These factors will cause monolayer Fe_2WX_4 to have valley Hall effect under an in-plane electric field (Fig. 3(c)). Since here a

certain crystal symmetry is a necessary condition for realizing the valley Hall effect, we call the valley Hall effect in monolayer Fe_2WX_4 as the crystal valley Hall effect. Therefore, the valley Hall effect without the T symmetry can be realized in altermagnetic materials.

Finally, we study the properties of monolayer Fe_2WX_4 under strain. According to the above analysis, both $\{E||M_{xy}\}$ and $\{C_2^\perp||C_{4z}\}$ spin symmetries can protect the energy band degeneracy at the high-symmetry X and Y points. If we apply anisotropic strain to break the $\{C_2^\perp||M_{xy}\}$ and $\{C_2^\perp||C_{4z}\}$ spin symmetries, which will result in band splitting at the high-symmetry X and Y points(Fig. 4(a)). If we apply compressive stress in the x direction, the spin-down band at the high-symmetry X point will be higher than the spin-up band at the high-symmetry Y point, which corresponds to the spin-down valley polarization (Fig. 4(a) and (b)). At this point, monolayer Fe_2WSe_4 is still a semiconductor. When the Fermi level is adjusted to an appropriate position, Fe_2WSe_4 will have a negative net magnetic moment M. Conversely, if we apply a tensile strain in the x direction, monolayer Fe_2WSe_4 will produce spin-up valley polarization and has a positive net magnetic moment $-M$ by adjusting the Fermi level. Similarly, valley polarization and piezomagnetic effects can be obtained by applying stress along the y direction (Fig. 4(b)). And our calculations also show that monolayer Fe_2WS_4 has similar properties. Therefore, both monolayer Fe_2WSe_4 and Fe_2WS_4 can realize piezomagnetic effects.

On the other hand, under biaxial compression stress, monolayer Fe_2WX_4 still has $\{C_2^\perp||M_{xy}\}$ and $\{C_2^\perp||C_{4z}\}$ spin symmetries. So the energy bands at high-symmetry
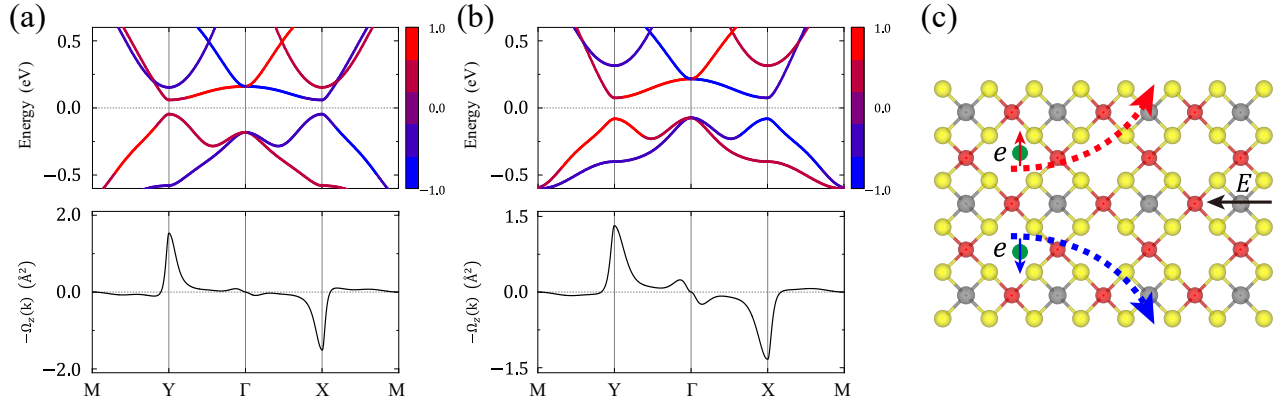
FIG. 3. Top panel: the electronic band structure of monolayer (a) Fe_2WSe_4 and (b) Fe_2WS_4 with the spin projection s_z; bottom panel: the corresponding berry curvature along the high-symmetry line. (c) The schematic diagram of crystal valley Hall effect in monolayer Fe_2WX_4. The E and e represent external electric field and electrons, respectively. The red and blue arrows represent up and down spins, respectively.
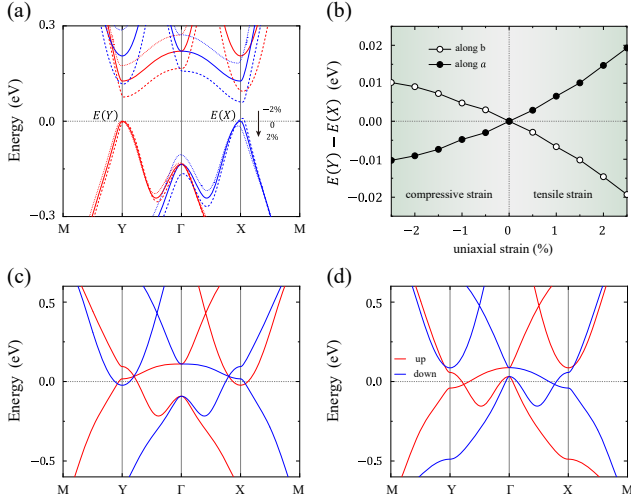

FIG. 4. Strain induced valley polarization and topological phase transition. (a) Band evolution under different uniaxial strains $(-2\%, 0, +2\%)$ along a direction. (b) Strain induced valley polarization, which defined as the energy difference between two valleys $E(Y) - E(X)$. (c) and (d) are the electronic band structure of Fe_2WSe_4 and Fe_2WS_4 along the high-symmetry directions, respectively.

X and Y points are still degenerate. Compressive strain can cause band broadening, so monolayer Fe_2WX_4 may induce band inversion under certain compressive strain due to small bandgap. Then, we can realize topological phase in monolayer Fe_2WX_4. To prove it, we calculated the electronic band structure of monolayer Fe_2WX_4 along the high-symmetry direction under 3% compression strain, which is shown in Fig. 4(c) and (d). From Fig. 4(c) and (d), both monolayer Fe_2WSe_4 and Fe_2WS_4 indeed produce band inversion under 3% compression strain. Moreover, both monolayer Fe_2WSe_4 and Fe_2WS_4

have two pairs of Weyl points protected by $\{E||C_{2x}\}$ and $\{E||C_{2y}\}$ spin symmetries near the Fermi level and the two pairs of Weyl points have opposite spin polarization (Fig. 4(c) and (d)). Thus, under compressive strain, both monolayer Fe_2WSe_4 and Fe_2WS_4 transform from semiconductor phase to bipolarized topological Weyl semimetal phase. Therefore, we can indeed realize topological phase in both monolayer Fe_2WSe_4 and Fe_2WS_4 by regulating strain.

In summary, based on spin symmetry analysis and the first-principles electronic structure calculations, we predict two two-dimensional altermagnetic semiconductors Fe_2WSe_4 and Fe_2WS_4 with magnetic transition temperatures above room temperature. More importantly, when considering SOC, both monolayer Fe_2WSe_4 and Fe_2WS_4 can realize crystal valley Hall effect. Since the magnetic transition temperatures of both monolayer Fe_2WSe_4 and Fe_2WS_4 exceed room temperature, the crystal valley Hall effect may be observed at room temperature. In addition, under uniaxial strain, both monolayer Fe_2WSe_4 and Fe_2WS_4 can achieve piezomagnetic effects. Under biaxial compression stress, both monolayer Fe_2WSe_4 and Fe_2WS_4 will transform from altermagnetic semiconductor phase to bipolarized Weyl semimetal phase. Therefore, our work not only proposes a new physical effect, crystal valley Hall effect, but also provides a good platform to study the crystal valley Hall effect.

[1] D. Xiao, W. Yao, and Q. Niu, Valley-contrasting physics in graphene: Magnetic moment and topological transport, Phys. Rev. Lett. **99**, 236809 (2007).

[2] D. Xiao, G.-B. Liu, W. Feng, X. Xu, and W. Yao, Coupled Spin and Valley Physics in Monolayers of MoS_2 and Other Group-VI Dichalcogenides, Phys. Rev. Lett. **108**, 196802 (2012).

[3] K. F. Mak, K. L. McGill, J. Park, and P. L. McEuen, The valley Hall effect in MoS_2 transistors, Science **344**, 1489 (2014).

[4] S. Hayami, Y. Yanagi, and H. Kusunose, Momentum-Dependent Spin Splitting by Collinear Antiferromagnetic Ordering, J. Phys. Soc. Jpn. **88**, 123702 (2019).

[5] L. Šmejkal, R. González-Hernández, T. Jungwirth, and J. Sinova, Crystal time-reversal symmetry breaking and spontaneous Hall effect in collinear antiferromagnets, Sci. Adv. **6**, eaaz8809 (2020).

[6] L.-D. Yuan, Z. Wang, J.-W. Luo, E. I. Rashba, and A. Zunger, Giant momentum-dependent spin splitting in centrosymmetric low-Z antiferromagnets, Phys. Rev. B **102**, 014422 (2020).

[7] I. I. Mazin, K. Koepernik, M. D. Johannes, R. González-Hernández, and L. Šmejkal, Prediction of unconventional magnetism in doped $FeSb_2$, Proc. Natl. Acad. Sci. U.S.A. **118**, e2108924118 (2021).

[8] L. Šmejkal, J. Sinova, and T. Jungwirth, Emerging Research Landscape of Altermagnetism, Phys. Rev. X **12**, 040501 (2022).

[9] L. Šmejkal, J. Sinova, and T. Jungwirth, Beyond Conventional Ferromagnetism and Antiferromagnetism: A Phase with Nonrelativistic Spin and Crystal Rotation Symmetry, Phys. Rev. X **12**, 031042 (2022).

[10] I. Mazin, Editorial: Altermagnetism—a new punch line of fundamental magnetism, Phys. Rev. X **12**, 040002 (2022).

[11] P.-J. Guo, Z.-X. Liu, and Z.-Y. Lu, Quantum anomalous hall effect in collinear antiferromagnetism, npj Comput. Mater. **9**, 70 (2023).

[12] R. González-Hernández, L. Šmejkal, K. Výborný, Y. Yahagi, J. Sinova, T. c. v. Jungwirth, and J. Železný, Efficient Electrical Spin Splitter Based on Nonrelativistic Collinear Antiferromagnetism, Phys. Rev. Lett. **126**, 127701 (2021).

[13] A. Bose, N. J. Schreiber, R. Jain, D.-F. Shao, H. P. Nair, J. Sun, X. S. Zhang, D. A. Muller, E. Y. Tsymbal, D. G. Schlom, and D. C. Ralph, Tilted spin current generated by the collinear antiferromagnet ruthenium dioxide, Nat. Electron. **5**, 267 (2022).

[14] H. Bai, L. Han, X. Y. Feng, Y. J. Zhou, R. X. Su, Q. Wang, L. Y. Liao, W. X. Zhu, X. Z. Chen, F. Pan, X. L. Fan, and C. Song, Observation of Spin Splitting Torque in a Collinear Antiferromagnet RuO_2, Phys. Rev. Lett. **128**, 197202 (2022).

[15] S. Karube, T. Tanaka, D. Sugawara, N. Kadoguchi, M. Kohda, and J. Nitta, Observation of Spin-Splitter Torque in Collinear Antiferromagnetic RuO_2, Phys. Rev. Lett. **129**, 137201 (2022).

[16] L. Šmejkal, A. B. Hellenes, R. González-Hernández, J. Sinova, and T. Jungwirth, Giant and Tunneling Magnetoresistance in Unconventional Collinear Antiferromagnets with Nonrelativistic Spin-Momentum Coupling, Phys. Rev. X **12**, 011028 (2022).

[17] R.-W. Zhang, C. Cui, R. Li, J. Duan, L. Li, Z.-M. Yu, and Y. Yao, Predictable gate-field control of spin in altermagnets with spin-layer coupling, Phys. Rev. Lett. **133**, 056401 (2024).

[18] D.-F. Shao, S.-H. Zhang, M. Li, C.-B. Eom, and E. Tsymbal, Spin-neutral currents for spintronics, Nat. Commun. **12**, 7061 (2021).

[19] D. Zhu, Z.-Y. Zhuang, Z. Wu, and Z. Yan, Topological superconductivity in two-dimensional altermagnetic metals, Phys. Rev. B **108**, 184505 (2023).

[20] L. Šmejkal, A. H. MacDonald, J. Sinova, S. Nakatsuji, and T. Jungwirth, Anomalous Hall antiferromagnets, Nat. Rev. Mater. **7**, 482 (2022).

[21] Z. Feng, X. Zhou, L. Šmejkal, L. Wu, Z. Zhu, H. Guo, R. González-Hernández, X. Wang, H. Yan, P. Qin, X. Zhang, H. Wu, H. Chen, Z. Meng, L. Liu, Z. Xia, J. Sinova, T. Jungwirth, and Z. Liu, An anomalous hall effect in altermagnetic ruthenium dioxide, Nat. Electron. **5**, 735 (2022).

[22] R. D. Gonzalez Betancourt, J. Zubáč, R. Gonzalez-Hernandez, K. Geishendorf, Z. Šobáň, G. Springholz, K. Olejník, L. Šmejkal, J. Sinova, T. Jungwirth, S. T. B. Goennenwein, A. Thomas, H. Reichlová, J. Železný, and D. Kriegner, Spontaneous Anomalous Hall Effect Arising from an Unconventional Compensated Magnetic Phase in a Semiconductor, Phys. Rev. Lett. **130**, 036702 (2023).

[23] X.-Y. Hou, H.-C. Yang, Z.-X. Liu, P.-J. Guo, and Z.-Y. Lu, Large intrinsic anomalous Hall effect in both Nb_2FeB_2 and Ta_2FeB_2 with collinear antiferromagnetism, Phys. Rev. B **107**, L161109 (2023).

[24] X. Zhou, W. Feng, X. Yang, G.-Y. Guo, and Y. Yao, Crystal chirality magneto-optical effects in collinear antiferromagnets, Phys. Rev. B **104**, 024401 (2021).

[25] X. Zhou, W. Feng, R.-W. Zhang, L. Šmejkal, J. Sinova, Y. Mokrousov, and Y. Yao, Crystal Thermal Transport in Altermagnetic RuO_2, Phys. Rev. Lett. **132**, 056701 (2024).

[26] Y.-X. Li, Y. Liu, and C.-C. Liu, Creation and manipulation of higher-order topological states by altermagnets, Phys. Rev. B **109**, L201109 (2024).

[27] Y.-X. Li and C.-C. Liu, Majorana corner modes and tunable patterns in an altermagnet heterostructure, Phys. Rev. B **108**, 205410 (2023).

[28] H.-Y. Ma, M. Hu, N. Li, J. Liu, W. Yao, J.-F. Jia, and J. Liu, Multifunctional antiferromagnetic materials with giant piezomagnetism and noncollinear spin current, Nat. Commun. **12**, 2846 (2021).

[29] P.-J. Guo, Y. Gu, Z.-F. Gao, and Z.-Y. Lu, Altermagnetic ferroelectric $LiFe_2F_6$ and spin-triplet excitonic insulator phase (2023), arXiv:2312.13911 [cond-mat.mtrl-sci].

[30] S. Qu, Z.-F. Gao, H. Sun, K. Liu, P.-J. Guo, and Z.-Y. Lu, Extremely strong spin-orbit coupling effect in light el-

ement altermagnetic materials (2024), arXiv:2401.11065 [cond-mat.mtrl-sci].

[31] C.-Y. Tan, Z.-F. Gao, H.-C. Yang, K. Liu, P.-J. Guo, and Z.-Y. Lu, Bipolarized weyl semimetals and quantum crystal valley hall effect in two-dimensional altermagnetic materials (2024), arXiv:2406.16603 [cond-mat.mtrl-sci].

[32] G. Kresse and J. Furthm:uller, Efficiency of ab-initio total energy calculations for metals and semiconductors using a plane-wave basis set, Comput. Mater. Sci. **6**, 15 (1996).

[33] P. E. Blöchl, Projector augmented-wave method, Phys. Rev. B **50**, 17953 (1994).

[34] J. P. Perdew, K. Burke, and M. Ernzerhof, Generalized Gradient Approximation Made Simple, Phys. Rev. Lett. **77**, 3865 (1996).

[35] A. A. Mostofi, J. R. Yates, Y.-S. Lee, I. Souza, D. Vanderbilt, and N. Marzari, wannier90: A tool for obtaining maximally-localised Wannier functions, Comput. Phys. Commun. **178**, 685 (2008).

[36] L. Liu, X. Ren, J. Xie, B. Cheng, W. Liu, T. An, H. Qin, and J. Hu, Magnetic switches via electric field in BN nanoribbons, Appl. Surf. Sci. **480**, 300 (2019).

[37] E. A. Pruss, B. S. Snyder, and A. M. Stacy, A New Layered Ternary Sulfide: Formation of Cu_2WS_4 by Reaction of WS_4^{2-} and Cu^+ Ions, Angew. Chem. Int. Ed. Engl. **32**, 256 (1993).

[38] C. J. Crossland, P. J. Hickey, and J. S. O. Evans, The synthesis and characterisation of Cu_2MX_4 (M = W or Mo; X = S, Se or S/Se) materials prepared by a solvothermal method, J. Mater. Chem. **15**, 3452 (2005).

[39] Y. Lin, S. Chen, K. Zhang, and L. Song, Recent Advances of Ternary Layered Cu_2MX_4 (M = Mo, W; X = S, Se) Nanomaterials for Photocatalysis, Solar RRL **3**, 1800320 (2019).

[40] R. Balu, S. K. Sundaram, S. Rameshkumar, K. Aravinth, and P. Ramasamy, Controlled growth of 2D structured Cu_2WS_4 nanoflakes for high-performance all-solid-state supercapacitors, J. Electroanal. Chem. **922**, 116718 (2022).

[41] P. D. Tran, M. Nguyen, S. S. Pramana, A. Bhattacharjee, S. Y. Chiam, J. Fize, M. J. Field, V. Artero, L. H. Wong, J. Loo, and J. Barber, Copper molybdenum sulfide: a new efficient electrocatalyst for hydrogen production from water, Energy Environ. Sci. **5**, 8912 (2012).

[42] F. Zhan, Q. Wang, Y. Li, X. Bo, Q. Wang, F. Gao, and C. Zhao, Low-Temperature Synthesis of Cuboid Silver Tetrathiotungstate (Ag_2WS_4) as Electrocatalyst for Hydrogen Evolution Reaction, Inorg. Chem. **57**, 5791 (2018).